

Multiferroism in strained strontium hexaferrite epitaxial thin films

Joonhyuk Lee,^{1,*} Sam Yeon Cho,^{2,*} Inhwan Kim^{1,*}, Christopher M. Rouleau³, Kungwan Kang,¹ Sangkyun Ryu¹,
Yunseok Heo,¹ Jong K. Keum³, Daniel M. Pajerowski,⁴ Younghak Kim⁵, Sang Don Bu^{2,†},
Jaekwang Lee^{1,‡} and Hyoungjeen Jeon^{1,§}

¹Department of Physics, Pusan National University, Busan 46241, South Korea

²Department of Physics, Jeonbuk National University, Jeonju 54896, South Korea

³Center for Nanophase Materials Sciences, Oak Ridge National Laboratory, Oak Ridge, Tennessee 37831, USA

⁴Neutron Scattering Division, Oak Ridge National Laboratory, Oak Ridge, Tennessee 37830, USA

⁵Pohang Accelerator Laboratory, POSTECH, Pohang, 37673, South Korea

 (Received 5 September 2023; revised 6 December 2023; accepted 12 January 2024; published 5 February 2024)

Ferrimagnetic SrFe₁₂O₁₉ (SrM) is a mother phase for ferrite permanent magnets, which are commonly used due to its low cost compared to that of Nd-based permanent magnets and broader uses in permanent magnet markets. Recently, its electronic ground state has been debated. It has been proposed that the SrM is in a quantum paraelectric state in its single-crystal form, while polycrystalline SrM is a ferroelectric state. In this work, strain can stabilize ferroelectricity at room temperature, while keeping its ferrimagnetism. The strained SrM shows not only clear magnetic hysteresis but also $\sim 4.4 \mu\text{C}/\text{cm}^2$ as remnant polarization. From high-temperature thermal annealing, its crystallinity and ferroelectricity are even strengthened. Those are visualized by significant reduction in full width at half maximum of the rocking curve and $\sim 7.9 \mu\text{C}/\text{cm}^2$ in remnant polarization. The results indicate this functionality can be discovered from old and well-known materials.

DOI: [10.1103/PhysRevMaterials.8.024401](https://doi.org/10.1103/PhysRevMaterials.8.024401)

I. INTRODUCTION

Hexaferrites have served as the backbone for ferrite permanent magnets [1,2]. Its lower cost compared to that of Nd-based magnet has made it popular in this sector of the markets. However, their intrinsically low saturation magnetization has always been considered to need improvement. To improve their magnetic properties, industrial approaches have been based on “alchemy”-based routes, which involve random substitution of elements such as Co, La, and Ba [1,2]. Industrial needs are primarily focused on the use of cost-effective elements, but until recently, the structure-property relationships have not been actively considered in this material. For example, since the magnetic ground state of most hexaferrites is ferrimagnetic (see Fig. 1), it should be possible to tune the magnetic exchange interaction through structural modifications from strain engineering [3–5].

Recently, hexaferrites have attracted attentions due to their possible multifunctionality. For example, several hexaferrites were discovered to have multiferroic property [6–9]. However, in *M*-type hexaferrite SrFe₁₂O₁₉ (SrM), the electronic ground state is still controversial [10–12]. Rowley *et al.* argued that due to quantum criticality, their ferroelectric Curie temperature should occur at cryogenic temperatures. In their work, they claimed that the uniaxial electric dipole mo-

ment along the *c* axis was due to off-equator displacements of Fe³⁺ in the FeO₅ lattice (see Fig. 1). However, quantum fluctuations prevent the onset of long-range ferroelectric ordering. However, Kostishyn *et al.* observed clear room-temperature ferroelectric hysteresis with $\sim 45 \mu\text{C}/\text{cm}^2$, which supports multiferroism in this material [11]. In addition, Tan *et al.* claimed oxygen treatment at moderate temperature enhanced its polarization value over $100 \mu\text{C}/\text{cm}^2$ at room temperature [12].

Given these observations, it is reasonable to assume that epitaxial strain may induce similar lattice distortions in SrM to promote ferroelectricity, as strain is known to be an active knob to perturb the electronic properties of perovskite-based complex oxides [13–16], for example.

In this work, we stabilized epitaxial (001) SrFe₁₂O₁₉ on (111) SrTiO₃ and observed robust ferroelectricity at room temperature. Due to the intrinsic difference in lattice constants between the film and the substrate, the films include a built-in substrate-induced strain. From density-functional theory (DFT), strain can stabilize ferroelectricity through off-centering of Fe ions. Thus, we conclude the SrFe₁₂O₁₉ epitaxial film is multiferroic.

II. EXPERIMENTAL DETAILS

A. Film growth

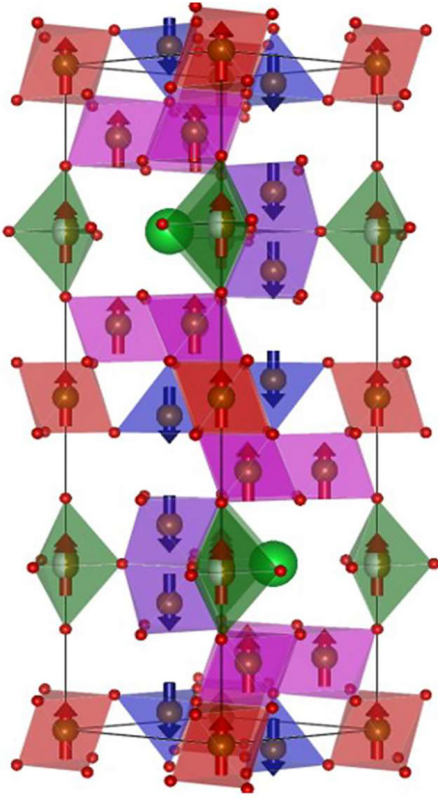
Pulsed laser deposition (PLD) was used to grow (001) SrFe₁₂O₁₉ (SrM) on (111) SrTiO₃ (STO) or (111) Nb-doped STO (0.5% Nb doping). To optimize the growth conditions, each film was grown at temperatures ranging from 650 °C

*These authors contributed equally to this work.

†sbu@jbnu.ac.kr

‡jaekwangl@pusan.ac.kr

§hjeen@pusan.ac.kr

FIG. 1. Atomic structure of SrFe₁₂O₁₉.

to 800 °C, oxygen partial pressures ranging from 0.005 to 100 mTorr, a laser of 2.2 mJ/cm², and a repetition rate of 10 Hz. A KrF excimer laser with a wavelength of 248 nm was used. The as-deposited films were cooled in the same growth oxygen partial pressure in which they were grown. The impurity-free and epitaxial films grown under optimal conditions (800 °C, 10 mTorr) were postannealed in air to enhance their crystallinity.

B. Film characterizations

For structural analysis, all the films were characterized with x-ray reflectivity, $\theta-2\theta$ scan, and ω rocking curves. Several samples were analyzed with φ scans to find the epitaxial relationship between the SrM film and STO substrate. Surface morphologies were also checked with atomic force microscope (AFM), particularly potential surface roughening due to high-temperature thermal annealing, and we found no significant surface roughening occurred in our SrM.

To determine valence state and metal-oxygen hybridization, x-ray absorption spectroscopy (XAS) of the Fe *L* edge and O *K* edge, and x-ray magnetic circular dichroism (XMCD) were performed using the 2A beamline at the Pohang accelerator laboratory. Elemental specific- and bulk magnetism were determined using the XMCD and a superconducting quantum interference device (SQUID) magnetometer (MPMS-3 from Quantum Design). Since SrM has strong crystalline magnetic anisotropy [17,18], all the magnetic information is from the out-of-plane direction, which is equivalent to the surface normal of the thin film. Sum rule was applied

to find element-specific spin magnetic moment (M_{spin}) and orbital magnetic moment (M_{orbital}). Details can be found in the previous works [19–21]. To determine potential multiferrimism in SrM, ferroelectric test and dielectric measurements were performed at room temperature. Dynamic hysteresis measurement technique was applied for the $P-E$ loops and $I-E$ curves with TF analyzer 2000 from AixACCT Co.

C. Theoretical calculations

Theoretical calculations were performed using the first-principles density-functional theory with the plane-wave based Vienna *Ab initio* Simulation Package (VASP) [22–24]. The revised Perdew, Burke, and Ernzerhof generalized gradient approximation is adapted for the exchange-correlation function [25]. We use the projector augmented-wave potentials that include 10 valence electrons for Sr ($4s^2$, $4p^6$, and $5s^2$) atom, 8 for Fe ($3d^7$ and $4s^1$) atom, and 6 for O ($2s^2$ and $2p^4$) atom [26]. The unit cell in our calculations has 2 Sr atoms, 24 Fe atoms, and 38 O atoms with the optimized lattice parameter of $a = b = 5.855$ Å, and $c = 22.831$ Å. A plane-wave cutoff energy of 600 eV is used and a Monkhorst-Pack grid with $8 \times 8 \times 2$ k -point mesh is used for the all calculations [27]. We use the nudged elastic band method to calculate the ferroelectric double-well potential-energy barrier [28]. We applied the onsite Hubbard- U correction of 4 eV to Fe using the Dudarev formalism [29]. We have considered the ferrimagnetic collinear spin ordering on the Fe atoms consisting of the up spin on the 2 bipyramidal and 14 octahedral Fe sites, whereas the down spin on the 4 octahedral and the 2 tetrahedral Fe sites, respectively. All calculations are converged in energy to 10^{-7} eV per unit cell and the structures are fully optimized with the forces convergence of 10^{-3} eV/Å.

III. RESULTS AND DISCUSSION

A. Structure of epitaxial SrM

Growth-condition optimization is based on structural characterization of the as-grown SrM thin films. Growth PO_2 and growth temperature (T_S) were used as parameters to optimize the epitaxial SrM thin films. Figure 2(a) shows that single-crystal epitaxial thin films are obtained in relatively narrow growth conditions, where the T_S is at 800 °C and PO_2 is between 1 and 10 mTorr. Figures 2(b), 2(c), and 2(d) show x-ray reflectivity (XRR), $\theta-2\theta$ scan, and φ scans from the c -axis oriented optimized thin film. XRR shows clear Kiessig fringes, and the thickness of the as-grown film was determined to be ~ 70 nm. Figure 2(c) shows the normal scan of the optimized SrM films, and it is clearly seen that the film is epitaxial and c -axis oriented without any impurities. The result is consistent with the previous report [30]. To elucidate the epitaxial relationship between SrM and STO, we performed φ scans of (201 $\bar{3}$) SrM and (220) STO, respectively. The results from (220) STO show threefold symmetry, while those from (201 $\bar{3}$) SrM show sixfold symmetry. In addition, the peak positions from the STO and the SrM coincide, confirming the heteroepitaxial growth of SrM thin films on 111 STO substrates with a (0001)[11 $\bar{2}$ 0] SrM//[(111)[1 $\bar{1}$ 0] STO.

Although the SrM thin films were epitaxial, the full width half maximum (FWHM) from the rocking-curve result of the

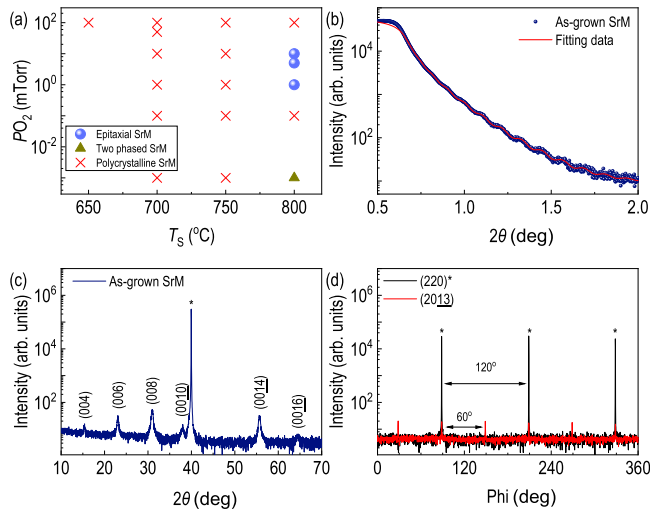


FIG. 2. (a) Growth-phase diagram of SrFe₁₂O₁₉ (SrM) epitaxial thin films on (111) SrTiO₃. Only filled blue circles are the condition for epitaxial thin films. (b) X-ray reflectivity and its fitting of epitaxial SrM thin film grown at the optimal growth condition. (c) X-ray diffraction of the epitaxial SrM thin film on (111) SrTiO₃. (d) Phi scans of (220) SrTiO₃ and (2013) SrM epitaxial thin film.

as-grown SrM was $\sim 0.7^\circ$, which is rather broad. In order to enhance the crystallinity of the SrM film, we postannealed several SrM samples in air using a muffle furnace. Figure 3(a) shows that with thermal annealing, the rocking-curve peak is sharpened, while the crystallinity does not deteriorate. Figure 3(b) shows the 0014 rocking curves. The FWHM value was reached down to $\sim 0.15^\circ$ when the film was annealed at 1100 °C. When we compared AFM images between the as-grown SrM and the annealed SrM at 1100 °C, the rms roughness (~ 1 nm) was essentially unchanged. Figures 3(c)

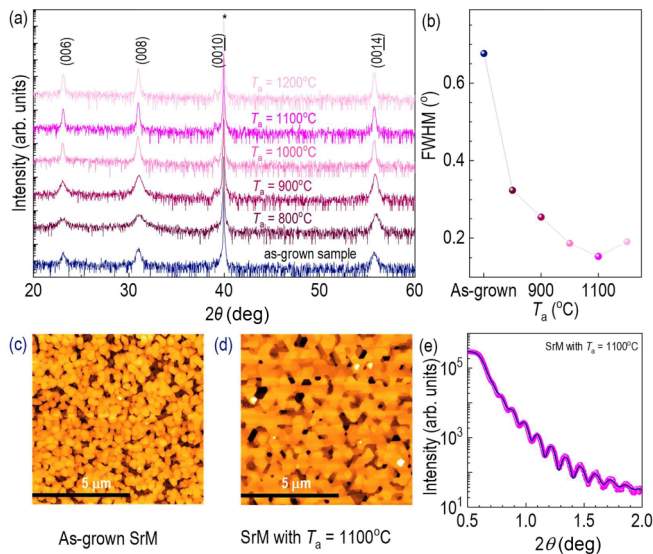


FIG. 3. (a) X-ray diffraction of epitaxial SrM thin films annealed at different temperatures in air. (b) Full width at half maximum of rocking curves from 0014 diffraction of SrM. Topographic images of (c) the as-grown SrM and (d) SrM annealed at 1100 °C. (e) X-ray reflectivity and its fitting of SrM annealed at 1100 °C.

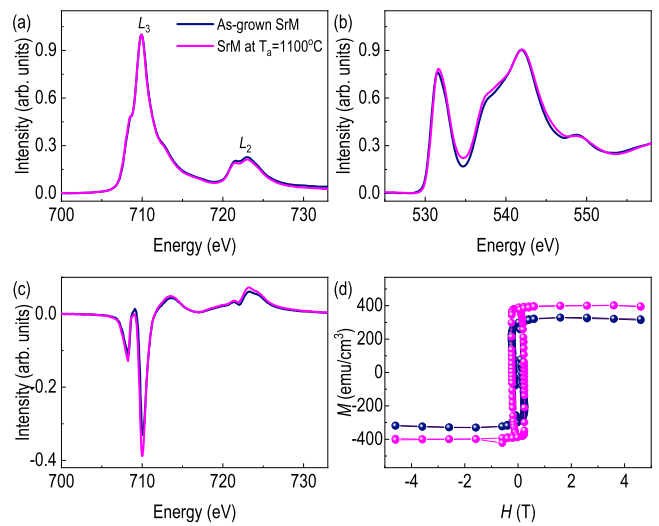


FIG. 4. X-ray absorption results are seen: (a) Fe *L*-edge spectra, and (b) O *K*-edge spectra of as-grown and annealed SrM epitaxial thin films. (c) X-ray magnetic circular dichroism of as-grown and annealed SrM epitaxial thin films at 0.5 T and 300 K. (d) Magnetic hysteresis curves of as-grown and annealed SrM epitaxial thin films at room temperature, when the magnetic field is parallel to film surface normal.

and 3(d) show that the grain growth occurs, and as a result we can claim that growth agglomeration in addition to enhanced crystallinity occurred. Note that we also observed the enhanced contrast in Kiessig fringes in x-ray reflectivity [see Fig. 3(e)].

B. Chemistry and magnetism of epitaxial of SrM

After confirming considerable changes in crystallinity in the annealed SrM, XAS was used to determine the valence state of Fe and metal-oxygen hybridization. XAS data from the Fe *L* edge show that the valence states of both the as-grown and the annealed SrMs are nearly identical. Especially, the *L*₂-edge spectrum consists of doublet, where each peak is closely related to the number of electrons in either *t*_{2g} and *e*_g levels in Fe ions [31]. The similar shape in the *L*₂-edge spectra indicates valence state are not changed, as shown in Fig. 4(a). From these results, the valence state of Fe ions in both SrMs is 3+. Thermal annealing does not lead to changes in valence, but only in crystallinity. XAS data from the O *K* edge were also obtained to see the changes in metal-oxygen hybridization. Both spectra near 532 eV show double-peak features, which originate from crystal-field splitting between *t*_{2g} and *e*_g sites [32]. Although we observed a slight increase of peak intensity near 532 eV, corresponding to Fe-O hybridization, overall the spectra are similar and indicate enhanced crystallinity does not lead to the dramatic changes in chemical state.

XMCD measurements were performed at room temperature in a 0.5-T magnetic field as shown in Fig. 4(c). The XMCD features are qualitatively similar to those of previously reported results [32]. Note that we clearly observed two dips and two peaks. The two dips are the magnetic signal originating from octahedral irons, while the peaks are the magnetic signal originating from tetrahedral irons [32]. These are

TABLE I. Magnetic moments from SQUID and XMCD of Fe *L*-edge spectra

	M_s from M vs H curves (μ_B/Fe)	M_{spin} from sum rule (μ_B/Fe)	M_{orbital} from sum rule (μ_B/Fe)	$M_{\text{spin}} + M_{\text{orbital}}$ (μ_B/Fe)
As-grown SrM SrM at $T_a = 1100$ °C	1.02	0.93	-0.03	0.90
	1.26	1.15	-0.01	1.14

aligned antiferromagnetically. As can be seen from Fig. 4(d), the coercive fields in our SrM films are less in 0.3 T and therefore XMCD in 0.5 T will reflect a magnetically saturated state. In both the SQUID and XMCD data, the saturated magnetic moment of the annealed SrM film is higher than that of the as-grown SrM film. Quantitatively, from M vs H curves, we calculated saturation magnetic moment in Bohr magneton per Fe. The values are $1.02 \mu_B/\text{Fe}$ for as-grown SrM and $1.26 \mu_B/\text{Fe}$. We adopted the sum rule [19,20] and calculated element-specific spin magnetic moment (M_{spin}) and orbital magnetic moment (M_{orbital}) from Fe *L*-edge XMCD. As seen in Table I, the M_{spin} from the annealed SrM is larger than that from the as-grown SrM film, while the M_{orbital} shows that the magnitude of the M_{orbital} is larger from the as-grown SrM. Since the M_{spin} and M_{orbital} are contributed in opposite way, the difference in overall magnetic moment from Fe *L*-edge XMCD spectra is further apart. The overall value is slightly smaller than that from the saturation magnetic moment; thus, we believe magnetism is mainly from the Fe sites and their interactions.

C. Ferroelectricity in epitaxial SrM

To check whether our SrM are ferroelectric, we measured dielectric constants and polarization-electric field (P - E) at room temperature. For realizing capacitor geometry, we grew SrM thin films on 0.5% Nb-doped SrTiO₃. With the Pt top electrode, we could form the capacitor geometry for the measurements of electrical properties. (We here note that such an asymmetric electrode structure can result in an asymmetry in the shape of a hysteresis loop such as imprint.) First, Figs. 5(a) and 5(b) show frequency dependence on dielectric constants and dissipation factors of as-grown and annealed thin films, respectively, from the multiple points in each film. As can be seen, both dielectric constant (ϵ) and dissipation factor [$\tan(\delta)$] are well matched. This indicates spatially uniform dielectric properties in each film. In addition, the dielectric constants are around 400 and 600 at 10^4 Hz for as-grown and annealed thin films, respectively, which are similar to those of SrM ceramics [12] and the small values (> 1) of dissipation factors suggest that the films has a high quality with low dielectric loss. Note that overall dielectric constant from the annealed SrM shows higher than that of the as-grown SrM.

Next, Figs. 5(c)-5(f) are P - E and current vs electric field (I - E) curves of each film. Even though each curve shows an asymmetric shape, as expected, distinct ferroelectric hysteresis curves were obtained for SrM thin films with driving voltages of up to 300 kV/cm. The increases in the remnant polarization (P_r) and the coercive field (E_c) with the driving voltage confirm that the SrM exhibit significant ferroelectric properties. The P_r of the as-grown SrM is thus

estimated to be $\sim 4.4 \mu\text{C}/\text{cm}^2$, while the P_r of the annealed SrM is $\sim 7.9 \mu\text{C}/\text{cm}^2$. In addition, the annealed SrM has the E_c value of 91 kV/cm, lower than that of as-grown film (144 kV/cm). More importantly, in the I - E curves, current peaks are clearly seen. This indicates direct displacement current peaks, which imply the presence of spontaneous polarization (P_s) switching. These show that our SrM films have some typical ferroelectric behavior [33]. Even if both as-grown and the annealed SrMs are ferroelectric, the annealed SrM has the higher remnant polarization (P_r). In I - E curves in Figs. 5(e) and 5(f); rather, broader peaks and dips near the zero field can be seen. It is likely that the broader peak and dip near zero bias are found in Mn and/or Fe-based multiferroic materials such as CoFe₂O₄-doped $_{0.94}\text{Na}_{0.5}\text{Bi}_{0.5}\text{TiO}_{3-0.06}\text{BaTiO}_3$ and YMnO₃. This is related to modulation in space-charge

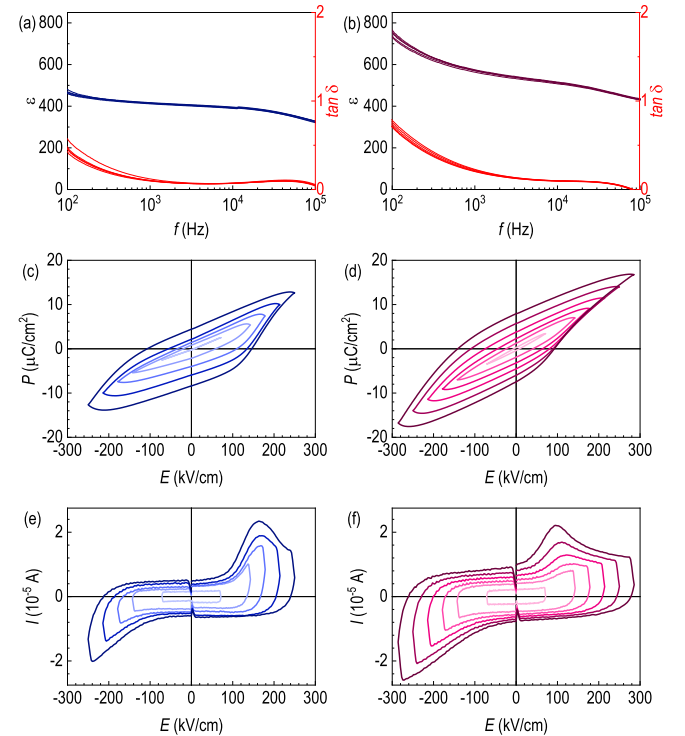


FIG. 5. Frequency-dependent dielectric constants (ϵ) and dissipation factors ($\tan \delta$) from (a) as-grown and (b) annealed SrM epitaxial thin films. Polarization (P) vs electric field (E) curves of (c) as-grown and (d) annealed SrM epitaxial thin films. Current (I) vs electric field (E) curves of (e) as-grown and (f) annealed SrM epitaxial thin films. For electrical measurements, (111) 0.5% Nb-doped SrTiO₃ substrates were used. All the measurements were taken at room temperature.

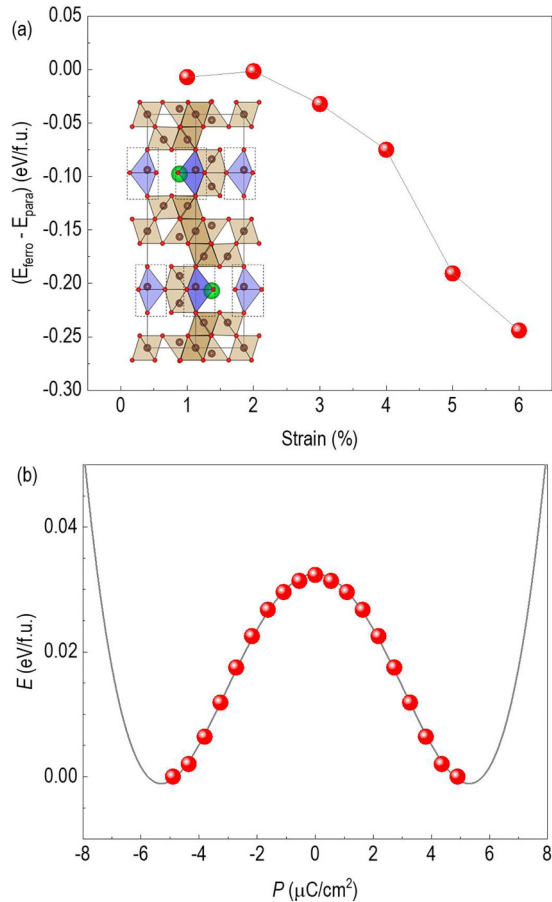


FIG. 6. (a) Energy difference between ferroelectric and paraelectric phase vs compressive strain. Inset shows atomic structure in stabilization of ferroelectric phase. (b) Energy vs polarization curve in stabilization of ferroelectric phase. Clear double-well potential is built.

polarization due to the fluctuation of transition metal's valence state [34,35].

D. Role of strain for ferroelectricity

To elucidate the physical origin of the ferroelectric behavior in ferrimagnetic strained SrM, we apply the biaxial

compressive strain along the in-plane direction. As shown in Fig. 6(a), the energy difference between ferroelectric and paraelectric phase always shows negative value, supporting that the ferroelectric state is energetically favorable under the biaxial compressive strain. We can see that the compressive biaxial strain generates the ferroelectric atomic displacements in paraelectric SrM and induces the phase transition to ferroelectric SrM. [see the inset of Fig. 6(a)]. Figure 6(b) shows the double-well potential for the 3% strained SrM. The energy barrier is estimated at about 0.03 eV per each formula unit, and the value of the electric polarization is $5 \mu\text{C}/\text{cm}^2$. Interestingly, even if Fe ions have been distributed in bipyramidal, octahedral, and tetrahedral sites, the ferroelectric atomic displacements have been induced only at the bipyramid sites. Such a selective response is unique in SrM and quite different from substrate-induced ferroelectricity observed in conventional ferroelectric complex oxides [14,36–38].

IV. CONCLUSION

In summary, we stabilized epitaxial (001) $\text{SrFe}_{12}\text{O}_{19}$ on (111) SrTiO_3 and observed robust ferroelectricity at room temperature. In addition, thermal annealing strengthens both ferroelectricity and magnetism by enhancing crystallinity. The stabilization of ferroelectricity under compressive strain is likely due to off-centering of Fe ions from DFT calculation. Since both ferrimagnetism and ferroelectricity are from the same element, a large magnetoelectric coupling [12] and its tuning by control of strain state is expected.

ACKNOWLEDGMENTS

This work was supported by National Research Foundation of Korea (Grant No. NRF-2018M2A2B3A01071859). PLD and XRD were conducted as part of a user project at the Center for Nanoscale Materials Sciences (CNMS), which is a U.S. Department of Energy, Office of Science User Facility at Oak Ridge National Laboratory. Partly, this work was financially supported by the 2022 Post-Doc. Development Program of Pusan National University. DFT calculation and XRD measurements were supported by Korea Basic Science Institute (National Research Facilities and Equipment Center) grant funded by the Ministry of Education (Grant No. 2021R1A6C101A429).

- [1] C. de Julián Fernández, C. Sangregorio, J. de la Figuera, B. Belec, D. Makovec *et al.*, *J. Phys. D: Appl. Phys.* **54**, 153001 (2021).
- [2] R. C. Pullar, *Prog. Mater. Sci.* **57**, 1191 (2012).
- [3] S. Shinde, R. Ramesh, S. Lofland, S. Bhagat, S. Ogale *et al.*, *Appl. Phys. Lett.* **72**, 3443 (1998).
- [4] Q. Zhu, R. Tang, F. Peng, S. Xu, G. Liang *et al.*, *Phys. Rev. Appl.* **16**, 054006 (2021).
- [5] C. Ederer and N. A. Spaldin, *Phys. Rev. B* **71**, 224103 (2005).
- [6] S. Trukhanov, A. Trukhanov, M. Salem, E. Trukhanova, L. Panina *et al.*, *Ceram. Int.* **44**, 21295 (2018).
- [7] S. Trukhanov, A. Trukhanov, V. Kostishyn, L. Panina, A. V. Trukhanov *et al.*, *J. Magn. Magn. Mater.* **442**, 300 (2017).
- [8] Y. S. Chai, S. H. Chun, J. Z. Cong, and K. H. Kim, *Phys. Rev. B* **98**, 104416 (2018).
- [9] G. Tan and X. Chen, *J. Magn. Magn. Mater.* **327**, 87 (2013).
- [10] S. E. Rowley, Y.-S. Chai, S.-P. Shen, Y. Sun, A. T. Jones *et al.*, *Sci. Rep.* **6**, 25724 (2016).
- [11] V. G. Kostishyn, L. V. Panina, A. V. Timofeev, L. V. Kozhitov, A. N. Kovalev *et al.*, *J. Magn. Magn. Mater.* **400**, 327 (2016).
- [12] G. Tan and H. Sheng, *PLoS One* **11**, e0167084 (2016).
- [13] A. Biswas, M. Rajeswari, R. C. Srivastava, Y. H. Li, T. Venkatesan *et al.*, *Phys. Rev. B* **61**, 9665 (2000).
- [14] K. H. Ahn, T. Lookman, and A. R. Bishop, *Nature (London)* **428**, 401 (2004).
- [15] A. J. Hatt and N. A. Spaldin, *Eur. Phys. J. B* **71**, 435 (2009).

- [16] K. A. Stoerzinger, W. S. Choi, H. Jeon, H. N. Lee, and Y. Shao-Horn, *J. Phys. Chem. Lett.* **6**, 487 (2015).
- [17] J.-H. Choy, Y.-S. Han, and S.-W. Song, *Mater. Lett.* **19**, 257 (1994).
- [18] B. D. Cullity and C. D. Graham, *Introduction to Magnetic Materials*, 2nd ed. (Wiley-IEEE Press, Hoboken, 2009).
- [19] B. T. Thole, P. Carra, F. Sette, and G. van der Laan, *Phys. Rev. Lett.* **68**, 1943 (1992).
- [20] C. T. Chen, Y. U. Idzerda, H. J. Lin, N. V. Smith, G. Meigs *et al.*, *Phys. Rev. Lett.* **75**, 152 (1995).
- [21] Y. Kim, S. Ryu, and H. Jeon, *RSC Adv.* **9**, 2645 (2019).
- [22] P. Hohenberg and W. Kohn, *Phys. Rev.* **136**, B864 (1964).
- [23] B. Y. Tong and L. J. Sham, *Phys. Rev.* **144**, 1 (1966).
- [24] G. Kresse and J. Furthmuller, *Phys. Rev. B* **54**, 11169 (1996).
- [25] J. P. Perdew, A. Ruzsinszky, G. I. Csonka, O. A. Vydrov, G. E. Scuseria *et al.*, *Phys. Rev. Lett.* **100**, 136406 (2008).
- [26] P. E. Blochl, *Phys. Rev. B* **50**, 17953 (1994).
- [27] H. J. Monkhorst and J. D. Pack, *Phys. Rev. B* **13**, 5188 (1976).
- [28] G. Henkelman, B. P. Uberuaga, and H. Jónsson, *J. Chem. Phys.* **113**, 9901 (2000).
- [29] S. L. Dudarev, G. A. Botton, S. Y. Savrasov, C. J. Humphreys, and A. P. Sutton, *Phys. Rev. B* **57**, 1505 (1998).
- [30] D. H. Kim, S. H. Han, Y.-M. Kang, D. Yang, and C. A. Ross, *J. Alloys Compd.* **692**, 545 (2017).
- [31] J. Lee, E. Ahn, Y.-S. Seo, Y. Kim, T.-Y. Jeon *et al.*, *Phys. Rev. Appl.* **10**, 054035 (2018).
- [32] G. D. Soria, P. Jenus, J. F. Marco, A. Mandziak, M. Sanchez-Arenillas *et al.*, *Sci. Rep.* **9**, 11777 (2019).
- [33] J. Kim, S. A. Yang, Y. C. Choi, J. K. Han, K. O. Jeong *et al.*, *Nano Lett.* **8**, 1813 (2008).
- [34] I. Fina, L. Fàbrega, E. Langenberg, X. Martí, F. Sánchez *et al.*, *J. Appl. Phys.* **109**, 074105 (2011).
- [35] M. Pal, A. Srinivas, and S. Asthana, *Physica B* **666**, 415127 (2023).
- [36] W. Prellier, A. Biswas, M. Rajeswari, T. Venkatesan, and R. L. Greene, *Appl. Phys. Lett.* **75**, 397 (1999).
- [37] P. R. Mickel, H. Jeon, P. Kumar, A. Biswas, and A. F. Hebard, *Phys. Rev. B* **93**, 134205 (2016).
- [38] R. Ramesh and N. A. Spaldin, *Nat. Mater.* **6**, 21 (2007).